Automated Quantitative Bone Analysis in *In Vivo* X-ray Micro-Computed Tomography

Ali Behrooz, Peet Kask, Jeff Meganck, and Joshua Kempner

***Abstract*— Measurement and analysis of bone morphometry in 3D micro-computed tomography volumes using automated image processing and analysis improve the accuracy, consistency, reproducibility, and speed of preclinical osteological research studies. Automating segmentation and separation of individual bones in 3D micro-computed tomography volumes of murine models presents significant challenges considering partial volume effects and joints with thin spacing, i.e., 50 to 100 μm. In this paper, novel hybrid splitting filters are presented to overcome the challenge of automated bone separation. This is achieved by enhancing joint contrast using rotationally invariant second-derivative operators. These filters generate split components that seed marker-controlled watershed segmentation. In addition, these filters can be used to separate metaphysis and epiphysis in long bones, e.g., femur, and remove the metaphyseal growth plate from the detected bone mask in morphometric measurements. Moreover, for slice-by-slice stereological measurements of long bones, particularly curved bones, such as tibia, the accuracy of the analysis can be improved if the planar measurements are guided to follow the longitudinal direction of the bone. In this paper, an approach is presented for characterizing the bone medial axis using morphological thinning and centerline operations. Building upon the medial axis, a novel framework is presented to automatically guide stereological measurements of long bones and enhance measurement accuracy and consistency. These image processing and analysis approaches are combined in an automated streamlined software workflow and applied to a range of *in vivo* micro-computed tomography studies for validation.**

***Index Terms*— Bone morphometry, hybrid thresholding, medial axis, object segmentation, splitting filters, stereological measurements, automated bone analysis, X-ray computed tomography.**

I. Introduction

BONE and osteological research, discovery, and treatment development studies rely extensively on analyses and measurements performed on *ex vivo* and *in vivo* three-dimensional (3D) anatomical images from X-ray micro-computed tomography (μCT) platforms [1]–[10]. Preclinical μCT imaging offers high spatial resolution (5-300 μm voxel size) for capturing anatomical details [4], [11]–[13] in addition to contrast between bone and soft tissue [4], [6], [12], [14]. As a result, μCT imaging is widely used for segmentation, characterization, quantification, and investigation of bone micro-architecture, formation, and diseases such as osteoarthritis, osteoporosis, and skeletal dysplasia, in a wide range of research efforts including cross-sectional, one-off, and longitudinal studies [2], [7], [15]–[18]. Measurements of bone morphometry enable quantitative observations into the biology of osteological tissue such as the characteristics of bone growth and loss as well as bone disease mechanisms and treatment development [19], [20]. Slice-by-slice stereological measurements of cortical and cancellous, *i.e.*, trabecular, compartments of long bones, *e.g.*, femur or tibia, are among the most widely used analytical workflows in osteological research. These measurements allow for quantitative screening and study of a range of bone morphometric and structural parameters, including cross-sectional area, thickness, and area moment of inertia, on a slice-by-slice basis along the longitude of a bone [14], [19], [21], [22]. The primary steps involved in quantifying bone morphometric parameters in *in vivo* μCT volumes include detection of the bone tissue, separation of the detected bone tissue into individual bones, segmentation of the trabecular and cortical compartments of individual bones, and 3D volumetric and stereological measurements of bone morphometry and micro-architecture.

Existing solutions for separation of individual bones in μCT volumes typically rely on manual operations in digitally interactive interfaces due to the absence of automated approaches [23], [24]. As such, studies involving bone separation are typically time-consuming and require laborious manual operations. Moreover, the accuracy and consistency of such studies is directly jeopardized by human operator variability and error [25]. Alternatively, in cases where manual separation is not available or speed of analysis is critical, 3D regions of interest (ROI) are extracted from parts of the μCT volume that only include the bone(s) under study. This ROI-based work-around, however, is significantly suboptimal in longitudinal studies as manually drawn 3D ROIs cannot consistently capture the entire bone or the same region of the bone under study across multiple longitudinal μCT scans. This imposes severe limitations on the scope of measurements and analyses that can be performed accurately using ROI-based analysis.

While there is a trend towards calculating structural parameters of the bone directly from 3D volumetric data

Manuscript received March 16, 2017; revised May 27, 2017; accepted May 30, 2017. Date of publication June 6, 2017; date of current version August 31, 2017. *(Corresponding author: Ali Behrooz.)*

A. Behrooz is with PerkinElmer, Inc., Hopkinton, MA 01748 USA (e-mail: alibehrooz@gatech.edu).

P. Kask, J. Meganck, and J. Kempner are with PerkinElmer, Inc., Hopkinton, MA 01748 USA.

Color versions of one or more of the figures in this paper are available online at http://ieeexplore.ieee.org.

Digital Object Identifier 10.1109/TMI.2017.2712571

rather than from separate 2D planes [26], there are certain parameters, such as area moment of inertia, that are quantified preferably by stereological measurements on a slice-by-slice basis [14], [22]. Existing methods for stereological quantification explicitly assume that a cardinal direction of the μCT scan is parallel to the principal axis of the bone under analysis. To perform slice-by-slice analysis on a bone in a μCT volume, the stack of 2D image slices are traversed along the x, y, or z directions of the volume [22], [23]. However, this approach is suboptimal and generates inaccurate measurements in the case of curved long bones, *e.g.* tibia, because the bone cross-sections used in the measurements follow a fixed direction that is not consistently aligned with the curved longitude of the bone.

In this work, a fully automated and optimized framework is presented for robust detection, separation, and morphometric analysis of bone morphometry in 3D μCT volumes. This framework requires no manual operations. Bone detection is performed using a hybrid thresholding approach which combines the advantages of global histogram-based thresholding [27] and local thresholding [28]. Automated separation of individual bones is performed on the detected bone mask using a novel approach based on second-derivative splitting filters that seed marker-controlled watershed segmentation. Even in cases where bones with different shapes are morphologically connected in the detected mask, the separation algorithm presented here can successfully separate the individual bones at typical μCT spatial resolutions (voxel size of 10 to 50 μm) with no user guidance or interaction. The algorithm overcomes the bone splitting challenge in scans with low spatial resolution, corresponding to voxel sizes larger than 20 μm, where partial volume effects are severe. Furthermore, we show that using the second-derivative splitting filters, the growth plate region of long bones, located beneath the epiphysis, can be automatically detected and excluded from cortical and trabecular morphometric analysis. This further improves the accuracy of a range of μCT-based bone morphometric analyses.

To guide slice-by-slice stereological measurements along the longitude of a bone, straight or curved in shape, a thinning-based approach is presented for obtaining the medial axis of an individual bone. The medial axis captures the longitudinal centerline of the bone. Stereological measurements of the bone cortical and trabecular compartments are applied to planes normal to the bone medial axis.

We present preclinical results from applying this automated framework to *in vivo* μCT scans of murine models. Structural parameters of long bones including femur and tibia are measured for μCT scans of small animals, with a wide range of spatial resolutions (voxel sizes of 5 to 80 μm).

II. Background

Detection of osseous tissue in μCT volumes is typically performed using manual or histogram-based global thresholding operations [23], [27] as discussed in Section I. However, these approaches generate poor or sub-optimal results [24], [28]. Partial volume effects cause artifacts in global thresholding techniques as these effects skew voxel

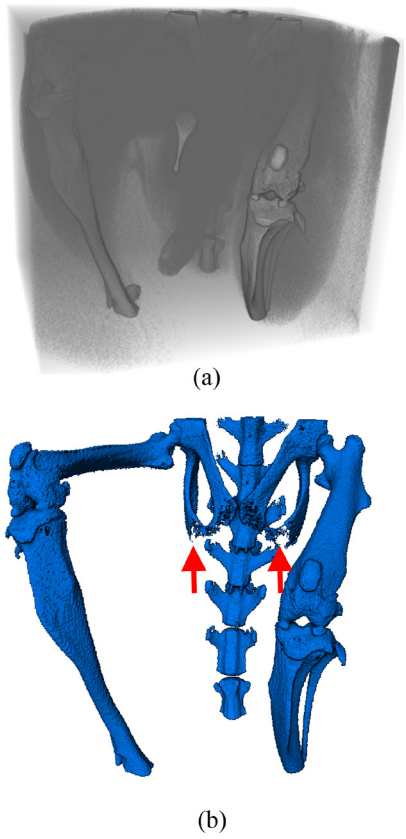

Fig. 1. Use of global thresholding for segmentation of bone from soft tissue generates suboptimal results especially for small and thin bone sections. a) The gray-scale μCT volume of the hindlimbs of a healthy mouse scanned at 46 μm voxel size and a field of view of 24 mm. b) In the binarized detected bone mask, artifacts of the global thresholding in detecting the ischium of the pelvic girdle are highlighted with red arrows.

intensity values. Partial volume effects are most significant in small bone structures or thin sections of bones, *e.g.*, trabecular bone or pelvic girdle, in μCT volumes with low voxel resolutions, i.e., 20 μm or larger in voxel size. An example is shown in Fig. 1 where the results of global thresholding in detecting bones in a μCT volume of a healthy murine model with 46 μm voxel size is depicted. As shown, histogram-based thresholding does not accurately detect the thin bone sections of the ischium in the pelvic girdles. The artifacts of global thresholding in detecting the pelvic girdles are highlighted in red arrows. To circumvent this problem, local thresholding approaches have been proposed for bone detection [28]. Local thresholding offers enhanced accuracy for detecting thin bone sections, but it is computationally expensive and time consuming. In this work, we present a hybrid thresholding approach that combines the benefits of global and local thresholding for improved accuracy and speed.

Automation of bone separation to accurately separate bones at locations of close proximity, such as the articulating surface within the hip joint, is challenging. Partial volume effects in thin joints, which span only a few voxels, cause adjacent bones to become morphologically connected in the detected bone mask. As a result, connected component analysis cannot accurately split and label the bones. A common approach in image processing to separate morphologically connected

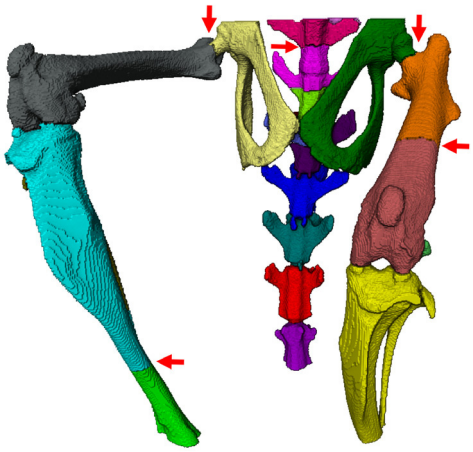

Fig. 2. The shortcomings of performing bone separation using traditional approaches such as watershed segmentation of the distance transform are highlighted using red arrows. Most notably, pelvis and femur are incorrectly separated at the narrowest connector rather than at the hip joint. Incorrect separation can also be noted in the vertebral joints.

segments is to apply watershed segmentation to the distance transform of the binary mask. This approach is widely used in object segmentation algorithms such as cell segmentation [29]. For 3D bone separation, however, this approach renders sub-optimal results as depicted in Fig. 2. In most other object segmentation cases the border of morphologically connected objects can be assumed to be on the narrowest or thinnest section of the binary object. However, as shown in Fig. 2, this is not the case for bone separation. As an example, the hip joint separates the femoral head and the acetabulum [30]. But the approach described above, which applies watershed to the distance transform, does not create a split line at the hip joint. Instead, it creates a false split line at the femoral neck, which connects the femoral head to the femoral shaft. These false split lines are highlighted by red arrows in Fig. 2. In this paper, we present novel splitting filters that overcome this challenge and split skeletal bones accurately.

Once the long bones are separated and their cortical and trabecular compartments segmented [31], 3D volumetric and stereological measurements of morphometric parameters can be performed on the whole bone or its compartments. These include measuring trabecular and cortical volume, surface area, thickness, and area moments of inertia [21], [22]. For stereological measurements, the spatial orientation of the cross-sectional image slices must be guided to follow the longitude of the bone. In existing workflows, the slices are aligned with one of the cardinal directions of the μCT volume. This approach generates cross-sections that can be oblique to the longitudinal direction of a curved bone and hence does not capture the bone stereology accurately as discussed in Section I. In this paper we present an approach for automatically guiding the cross-sectional slices using the concept of medial axis.

III. Methodology

The fully automated workflow presented in this paper for 3D volumetric and stereological analysis of bones in *in vivo* μCT volumes is comprised of four major steps: detection of osseous tissue, separation of individual bones, segmentation of cortical and trabecular compartments, and 3D volumetric and stereological measurements of bone morphometry. The methodology used for each of these steps is described below.

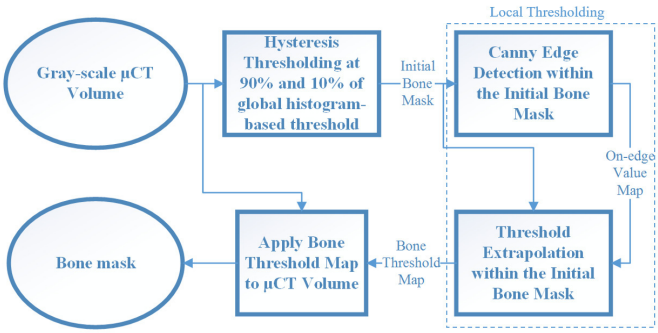

Fig. 3. The steps for performing bone detection using hybrid thresholding are outlined in this flowchart. By establishing a preliminary bone mask using hysteresis thresholding, the search space used in local thresholding can be limited to only inside the initial mask. This ensures speed and performance efficiency.

A. Bone Detection

The approach used in this work for segmenting bone from soft tissue in a μCT volume and generating a bone mask is summarized in a flow-chart in Fig. 3. After calibration of voxel intensity values into Hounsfield units [32] and thresholding out voxels with values below zero, a global threshold is determined automatically based on the voxel intensity histogram [27]. The global threshold is used in a hysteresis thresholding operation [33] that is applied to the μCT volume. The output of this operation is a preliminary binary mask that contains all the bone voxels in addition to some adjacent soft tissue voxels. This preliminary mask is then refined using local thresholding [28] as described in the flow-chart in Fig. 3.

Local thresholds are obtained by extrapolation of voxel intensity values on the computed edges [28] of the grayscale μCT volume. In this work, the edge detection and extrapolation steps are carried out only within the initial bone mask generated by hysteresis thresholding. This ensures computational speed and efficiency. The illustration in Fig. 4 depicts the result from this bone detection algorithm, which is described in detail in the flow-chart of Fig. 3, when applied to the μCT scan from Fig. 1 that includes the hind limbs of a healthy murine model imaged at a voxel size of 46 μm and field of view (FOV) of 24 mm.

B. Bone Separation

Once bone tissue is successfully segmented from soft tissue, and a binary bone mask is created to store the location of bone voxels within the μCT volume, the individual bones, *e.g.*, femur, tibia, or vertebrae, need to be separately labeled. This is needed as osteological studies are mostly focused on the morphometric and density characteristics of individual bones or compartments of individual bones.

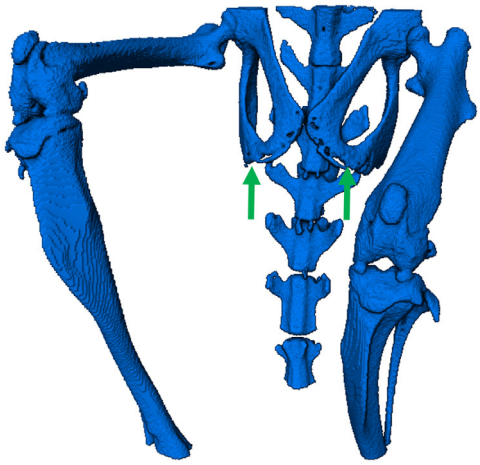

Fig. 4. The result of bone detection using hybrid thresholding. The artifacts present in global thresholding (illustrated in Fig. 1) are resolved as shown by green arrows, and the ischium of the pelvic girdle is successfully detected.

As discussed in Section II, voxels belonging to different individual bones can be morphologically connected, rather than separated, in the binary mask created by the bone detection step. This poses a challenge to performing automated bone separation simply because applying connected component analysis to the binary bone mask does not provide accurate bone separation. This problem is especially challenging in μCT scans with larger voxel size (*i.e.*, above 20 μm). Because of partial volume effects, bones become morphologically connected to each other in locations of close proximity, *i.e.*, at joints. To overcome this challenge in bone separation, we present a novel approach which employs rotationally invariant splitting filters to robustly locate the bone joints in μCT volumes and split individual bones. The role of splitting filters is to identify the location of skeletal joints and create split lines at joint locations in the binary bone mask. This will morphologically split neighboring bones. The splitting filters are defined based on the second-order spatial derivatives of the voxel intensities of the gray-scale μCT volume. The advantage of rotationally invariant filters is that they make splitting independent of bone orientation. These rotational invariants are obtained from the Hessian matrix calculated at each voxel of the μCT volume. Hessian matrix and its eigenvalues are described by

$$H(x,y,z) = \begin{bmatrix} \frac{\partial^2 I}{\partial x^2} & \frac{\partial^2 I}{\partial x \partial y} & \frac{\partial^2 I}{\partial x \partial z} \\ \frac{\partial^2 I}{\partial y \partial x} & \frac{\partial^2 I}{\partial y^2} & \frac{\partial^2 I}{\partial y \partial z} \\ \frac{\partial^2 I}{\partial z \partial x} & \frac{\partial^2 I}{\partial z \partial y} & \frac{\partial^2 I}{\partial z^2} \end{bmatrix} = V \begin{bmatrix} \sigma_1 & 0 & 0 \\ 0 & \sigma_2 & 0 \\ 0 & 0 & \sigma_3 \end{bmatrix} V^*, \quad (1)$$

where H is the Hessian matrix at a voxel with coordinates x, y, and z, I denotes the voxel intensity of the gray-scale μCT volume, V denotes the matrix containing the eigenvectors of H, and σ_1, σ_2, and σ_3 denote the highest, middle, and lowest eigenvalues of H, respectively. The eigenvalues of the Hessian matrix are independent of image orientation and hence capture rotationally invariant measures of the second-order partial derivatives. The measures used in the filters are the Laplacian (*LAP*), the highest eigenvalue of the Hessian (*HEH*) and the lowest eigenvalue of the Hessian (*LEH*), formulated as

$$LAP(x,y,z) = \frac{\partial^2 I}{\partial x^2} + \frac{\partial^2 I}{\partial y^2} + \frac{\partial^2 I}{\partial z^2} = \sigma_1 + \sigma_2 + \sigma_3,$$
$$LEH(x,y,z) = \sigma_3, HEH(x,y,z) = \sigma_1. \quad (2\text{-}4)$$

Each of these rotational invariants can be used as a texture filter. Among them, the Laplacian is one which can be calculated without solving the eigenvalue problem. Thus the *LAP* filter offers speed advantages over the others as it is simply calculated directly from the trace of the Hessian matrix. The *LAP* and *HEH* are used in the bone splitting filters. The *LEH* is used for growth plate filtering as discussed in Section III.C. The reason behind choosing *LAP* and *HEH* as the filters for bone splitting is that the expected pattern of the grayscale intensities of the voxels in a bone joint is concave. This is because the voxels within the joint gap are expected to have lower grayscale values compared to the neighboring bone voxels. Since second-order spatial derivatives are sensitive to concave patterns, they are adequate for identifying and locating joint voxels. The Laplacian describes the extent and sign of concavity, *i.e.*, concave up vs. concave down, of a given voxel in its neighborhood. In the joint, *i.e.*, the spatial gap between two bones, the voxel intensity is expectedly lower than the neighboring voxels belonging to the bones. This results in a concave-up intensity distribution making the Laplacian expectedly positive. This is illustrated in Fig. 5 which depicts a slice of a μCT volume (46 μm voxel size) containing the hip joint connecting femur and pelvis and the Laplacian of the image. The highest Hessian eigenvalue is also sensitive to the gap between bones as it quantifies the second-order partial derivatives of intensity distribution along directions with highest concavity. The lowest Hessian eigenvalue is sensitive to concave-down patterns and becomes useful in growth plate detection as discussed in Section III.C. The *LAP* and *HEH* splitting filters can be combined to form a hybrid splitting filter which identifies and removes voxels

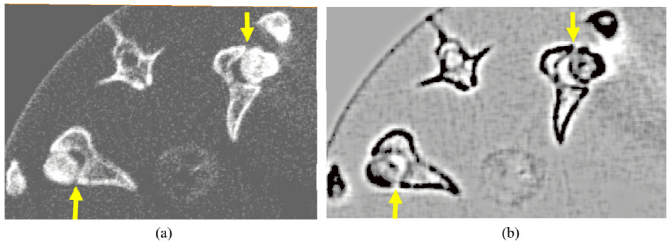

Fig. 5. The power of *LAP* and *HEH* splitting filters in separating thin joints comes from the improved joint contrast in the second-order spatial derivative space of the grayscale μCT volume. The second-order derivatives are sensitive to concave patterns which are expected in bone joints. a) A slice of the grayscale μCT volume containing the hip joints. b) The same slice from the *LAP* volume (Laplacian of the grayscale μCT volume). The *LAP* volume offers improved contrast in the hip joints compared to grayscale μCT volume as indicated by yellow arrows.

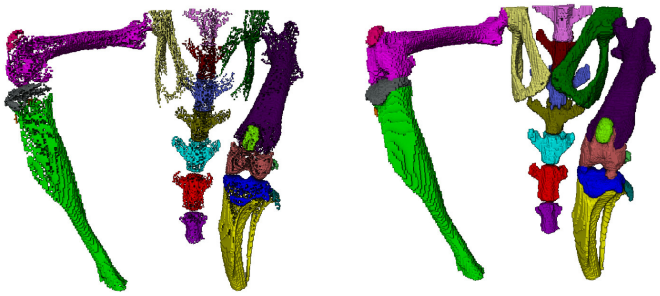

Fig. 6. Hybrid *LAP/HEH* splitting filter provides fully automated bone separation. a) Connected components of the output of the *LAP/HEH* splitting filter are labeled and used as seeds for marker-controlled watershed segmentation. b) The result of applying marker-controlled watershed segmentation to the inverted grayscale μCT volume using the seeds from part (a).

with a high *LAP* or *HEH* value from the binary bone mask. The result is a split bone mask in which the joint voxels have been removed and neighboring bones in close proximity have been morphologically disconnected.

The cut-off thresholds in splitting filters control the level of splitting. These need to be adjusted depending on the spatial resolution of the μCT volume to avoid over- and under-splitting. Once a splitting filter is applied to the binary bone mask, the connected components of the split binary bone mask are automatically identified [34] as shown in Fig. 6(a). These connected components are used as seeds in a marker-controlled watershed segmentation [35] applied to the grayscale μCT volume. By applying the binary bone mask to the split catchment basins of the watershed operation, a labeled bone mask is obtained as shown in Fig. 6(b). This is the final result of the bone separation step.

The operations described for bone separation in this section are summarized in a flow-chart illustrated in Fig. 7.

C. Compartment Segmentation

After separating individual bones in the μCT volume, measurements can be performed on the entire bone or separately on its cortical and cancellous compartments. For μCT scans of murine models**,** measurements of cortical and cancellous bone compartments are only applicable to volumes with voxel sizes of 20 μm or smaller. The approach used in this work for automated compartment segmentation relies on morphological operations from an algorithm reported in prior publications [31]. While this algorithm provides robust compartment segmentation, it requires an additional step when processing long bones, such as the tibia or femur, for a range of murine models. This additional step is required for removing the bone growth plate from the cortical compartment. The result of applying the previously reported compartment segmentation algorithm [31] to the tibia of a murine knee joint in a μCT volume with a voxel size of 10 μm and FOV of 5 mm is shown in Fig. 8. As illustrated in Fig. 8(b), the growth plate of the tibia comes out labeled as part of the cortical compartment. Here we report an automated technique for filtering out the growth plate from the cortical compartment mask.

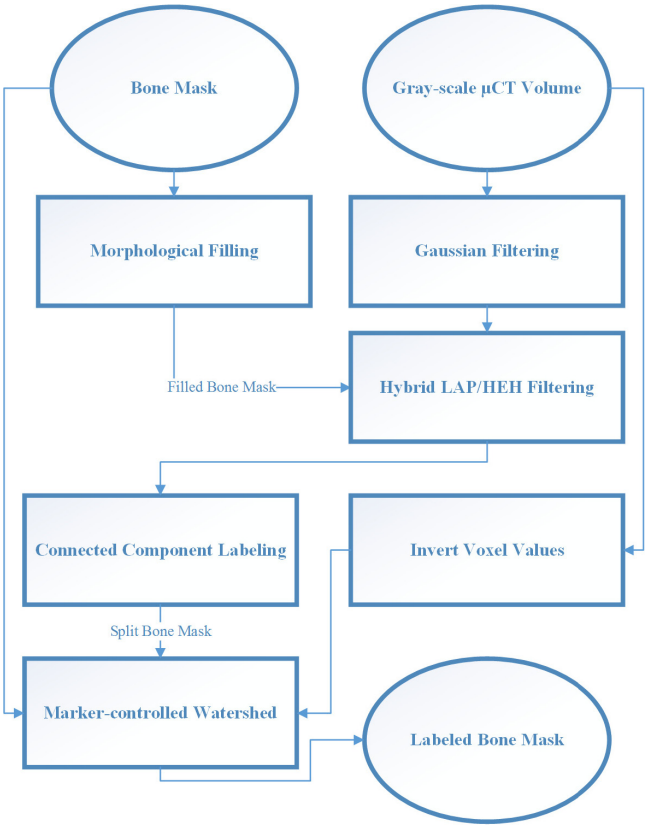

Fig. 7. Flow-chart showing steps involved in performing bone separation with splitting filters using the grayscale μCT volume and the binary bone mask. By applying hybrid *LAP/HEH* splitting to the binary bone mask, the bone will be separated at the joints. As a result, the connected components of the split bone mask can seed marker-controlled watershed to generate a correctly labeled bone mask.

This is done using the *LEH* filter described in Section III.B. By applying the *LEH* filter to the μCT volume, the growth plate can be identified and removed from the binary mask of the cortical compartment as depicted in Fig. 8(c). As discussed in Section III.B, the *LEH* filter is sensitive to concave-down patterns. As such, it can locate the growth plate region in the μCT volume where voxel intensities follow a concave-down distribution. The growth plate filtering results in an accurate segmentation and labeling of cortical and cancellous compartments of the long bones.

As described earlier, the growth plate removal algorithm is applied as a separate step after the preliminary compartment segmentation. Hence, this step can be skipped in the μCT scans of animal models with no identifiable growth plates. This is illustrated in Fig. 9 where compartment segmentation is applied to a μCT scan of a healthy 14-month old adult murine model. The scan has an FOV of 10 mm and voxel size of 20 μm. As shown in Fig. 9, the compartment segmentation can be used separately from the growth plate removal in cases where the latter is not needed.

D. Morphometric Measurements

Morphometric measurements include quantification of volume, boundary area, connectivity, and other structural, geometrical, and topological attributes of cortical and cancellous compartments of an individual bone [21]. Some of the

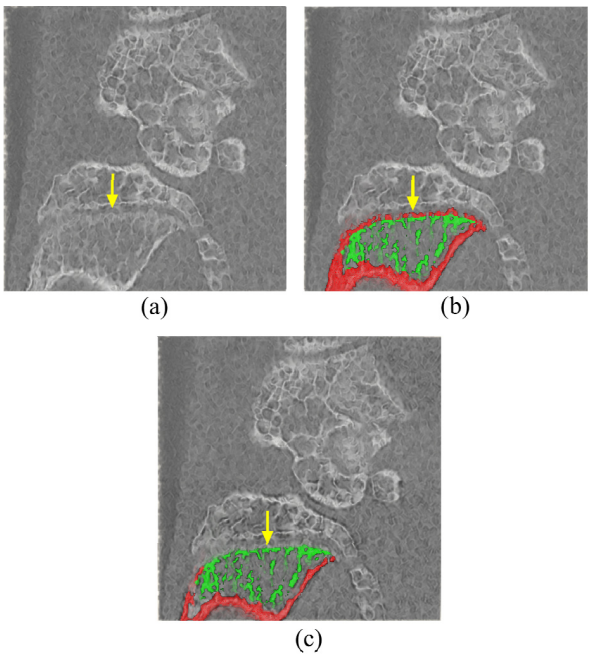

Fig. 8. Using *LEH* filtering, the growth plate can be automatically removed from the cortical compartment of long bones, such as tibia, as indicated by the yellow arrow. a) A slice of the grayscale μCT volume containing a knee joint of a murine model scanned at a voxel size of 10 μm and FOV of 5 mm is shown. b) Segmented cortical and cancellous compartments of the tibia, labeled in red and green, respectively, are overlaid with the grayscale slice. c) Segmented cortical and cancellous compartments, after growth plate removal by *LEH* filtering, are overlaid with the grayscale slice.

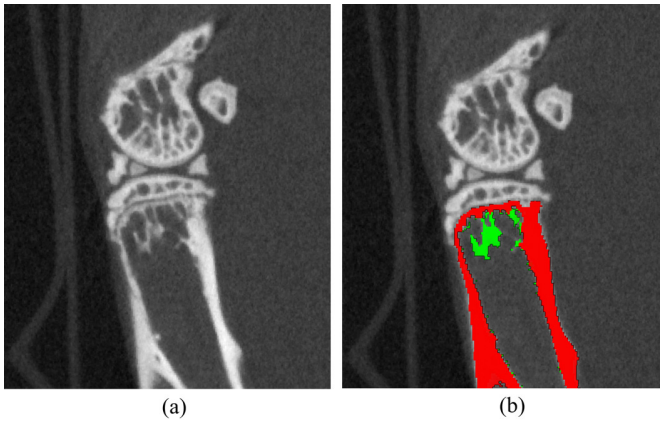

Fig. 9. Compartment segmentation is applied to a μCT volume of an adult murine model (14 months old) scanned at 10-mm FOV and 20-μm voxel size. a) A cross-section of the grayscale μCT volume is shown. b) Segmented cortical and cancellous compartments of the tibia, labeled in red and green, are overlaid with the grayscale cross-section.

key morphometric parameters used in osteological studies are stereological measures which require slice-by-slice processing and measurements [21], [22]. As discussed in Section II, in current bone analysis workflows [23], [36], these measurements are performed either along one of the cardinal directions of the μCT volume containing the bone or along the principal axis of a bone. These approaches result in inaccurate quantifications in the case of curved long bones, *e.g.*, tibia. In this work we present a novel approach for performing automated stereological measurements on long bones using the concept of medial axis. In this approach, the slice-by-slice

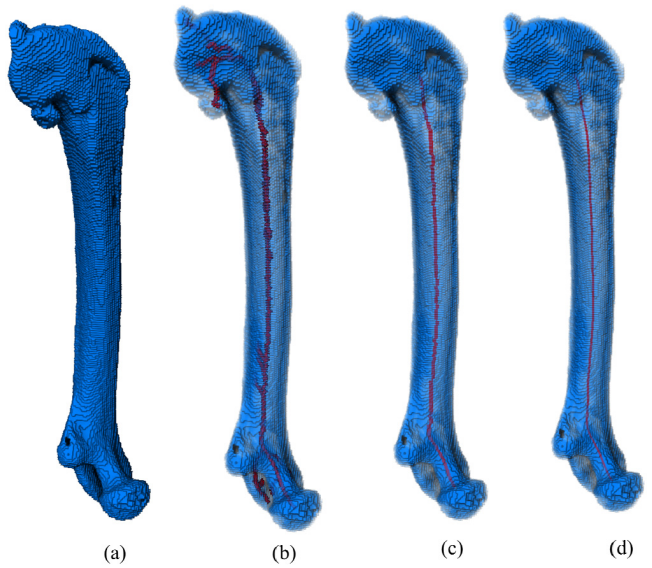

Fig. 10. Characterization of the medial axis for a murine femur using morphological thinning, pruning, and smoothing. a) Binary representation of the femur after morphological filling. b) The red structure, overlaid with the binary representation of the bone, depicts the result of 3D skeletonization applied to the filled femur volume. c) Pruning is applied to the 3D skeleton, using centerline tree operation, to remove non-major branches and generate a single-branched medial axis. d) The medial axis is smoothed to minimize uneven protrusions and artifacts.

measurements are guided by a medial axis that traverses the longitude of the bone and hence offers improved accuracy for curved long bones.

The bone medial axis is computed in three general steps. In the first step, the binary mask of the bone is morphologically filled, *i.e.*, the interior or marrow compartment is added to the bone mask to make it a non-hollow solid binary object. In the second step, skeletonization is performed on the filled bone by iterative 3D thinning [37]. In the third step, the main branch of the skeleton is identified by finding the centerline tree of the skeleton [38] and then smoothed. These three steps yield a single-branched medial axis that follows the central path of a bone as shown in Fig. 10 in which the steps for characterizing the medial axis of the right femur in the μCT volume of the hind limbs of a healthy mouse, scanned at 24-mm FOV and 46-μm voxel size is illustrated.

The flow-chart in Fig. 11 details the steps described above for characterizing the medial axis. As depicted in Fig. 10, the medial axis successfully captures the curves in both ends of the femur.

Once the medial axis of the bone is available, it can be used to guide the stereological measurements. The planes perpendicular to the medial axis are used to generate 2-D image slices of the cross-sections of the bone. Stereological measurements, *e.g.*, average cortical thickness or area moments of intertia, can be obtained from these 2-D cross-sections. To avoid measurement overlap between neighboring planes in curved parts, the distance pitch between the cross sections is adjusted based on the curvature of the medial axis.

In addition to stereological analysis, 3D volumetric measurements can also be performed on cortical and cancellous compartments of the bone. The 3D volumetric measurements

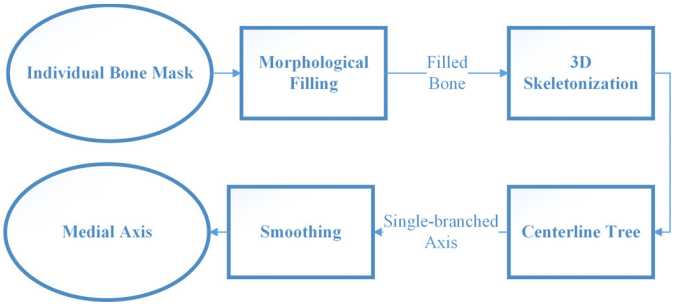

Fig. 11. The steps involved in characterizing the medial axis of a long bone are listed in a flow-chart. After the bone binary mask is filled morphologically, 3D skeletonization is applied to the filled bone mask. The 3D skeleton is then pruned using centerline tree operation. This results in a single-branched axis as depicted in Fig. 10. Finally, the axis is smoothed to generate a medial bone axis.

are not performed in a slice-by-slice manner, and hence can be directly applied to the volumes of the segmented compartments of a bone.

IV. Results

The automated bone analysis framework described in Section III was applied to μCT volumes from *in vivo* scans of knee joints, hind limbs, and whole bodies of murine models. The μCT system used for preclinical imaging in this work is the Quantum® FX platform (Rigaku, Inc.). This system offers *in vivo* partial and whole small animal X-ray imaging and computed tomography [39]. The average dose for a full μCT scan by this system is around 16 mGy [39] and the scan duration averages about 2 minutes. The scan is performed while the animal is under anesthesia.

The μCT volumes used for validation in this work included scans of knee joints of murine models at voxel sizes of 10 and 20 μm voxel (*i.e.*, small FOV of 5 and 10 mm), scans of hind limbs of murine models at a voxel size of 58 μm (30 mm FOV), and whole-body scans at a voxel size of 72 μm (90 mm FOV). In Fig. 12, results from the steps of bone detection and separation, in addition to the gray-scale volumes, are illustrated for the small-FOV datasets described above. As expected, the entire volumes of femur and tibia are not fully captured in these scans since the FOV is limited. In addition to the femur and tibia, the patella and the nodules in the knee joint are captured in these small-FOV scans.

As depicted in Fig. 12, the hybrid thresholding and splitting filters perform adequately in detecting and separating the bones, respectively. It must be noted that before performing compartment segmentation on the labeled masks of long bones such as femur and tibia, further splitting is required to segment the epiphysis of the long bone from the metaphysis. This is because the morphometric analysis of the metaphysis segment must be carried out separate from the epiphysis [40]. The bone splitting filters described in Section III.B, with proper parameterization, can perform the epiphysis-metaphysis separation as depicted in Figs. 12(g) and 12(h). This is achieved by increasing the cut-off levels of the hybrid *LAP/HEH* splitting filter.

After successful bone and epiphysis-metaphysis separation, the compartment segmentation and growth plate filtering

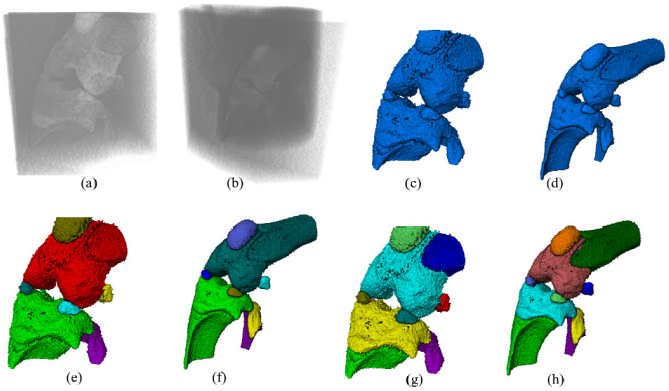

Fig. 12. Bone detection and separation are applied to μCT volumes of the knee joints of healthy murine models scanned at 5 mm and 10 mm FOVs with voxel sizes of 10 μm and 20 μm, respectively. The grayscale μCT volumes are depicted in parts (a) and (b). The segmented bone masks are depicted in parts (c) and (d). The labeled bone separation results are depicted in parts (e) and (f), where the femur, tibia, patella, fibula, and joint nodules are separated. Further splitting can be applied to the tibia and femur to separate the epiphysis and metaphysis components of the long bones as illustrated in parts (g) and (h).

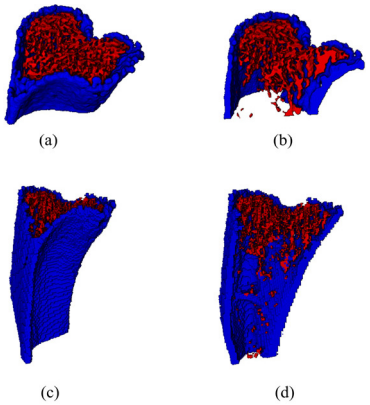

Fig. 13. Compartment segmentation and growth plate removal is applied to the μCT volumes with voxel sizes of 10 μm and 20 μm from Fig. 12. Cortical compartment is labeled in blue and trabecular (cancellous) compartment in red. Parts (a) and (b) illustrate the results for the scan at 10 μm voxel size and parts (c) and (d) for the scan at 20 μm voxel size.

operations, described in Section III.C, are applied to the metaphyseal section of the bone. The results are depicted in Fig. 13 where the cortical and trabecular compartments of the bone are labeled separately.

In the final step of the workflow, 3D morphometric measurements are performed on both compartments of the bone. We have used standardized morphometric parameters recommended by the American Society of Bone and Mineral Research (ASBMR). For proof of concept, we have applied the ASBMR morphometric measurements to the compartments of the tibia from the μCT volumes depicted in Fig. 13. The results are listed below in Table I.

The ASBMR morphometric parameters listed in Table I include volume, thickness, and average area of cortical and trabecular compartments in addition to trabecular surface area. These parameters are widely used in osteological studies as quantitative descriptors of in bone microarchitecture and structure. Changes in volume or average thickness in each compartment can reveal and quantify bone loss, growth, or progression

TABLE I
MORPHOMETRIC MEASUREMENTS OF MOUSE TIBIA IN SMALL-FOV DATA

Symbol	Parameter	Measured Value 5 mm FOV 10 μm Voxel Size	Measured Value 10 mm FOV 20 μm Voxel Size
Tb.BV	Trabecular Volume	0.715 mm^3	0.869 mm^3
Ct.TV	Cortical Volume	1.44 mm^3	4.95 mm^3
Tb.BS	Trabecular Surface	34.6 mm^2	40.6 mm^2
Tt.Ar	Total Area	1.28 mm^2	1.68 mm^2
Ct.Ar	Cortical Area	0.431 mm^2	0.993 mm^2
Ct.Th	Cortical Thickness	0.0699 mm	0.0939 mm
Tb.Th	Trabecular Thickness	0.0751 mm	0.0534 mm

of diseases such as osteoporosis [14]. It should be clear from the results depicted in Fig. 13 that the values of some of these morphometric measurements, such as cortical volume, will directly depend on the FOV. As listed in Table I, however, this is less pronounced for measurements of the trabecular compartment of the tibia. This is because the bulk of the trabeculae is located directly beneath the growth plate area and is therefore captured in both 5 mm and 10 mm FOV scans. The changes in the average thickness measurements between 5 mm and 10 mm FOV scans are also expected as scans with different FOVs do not capture the same regions of the cortical and trabecular compartments.

In scans with wide fields of view (larger than 10 mm), the bones belonging to the hind limbs or the entire mouse body, including vertebrae, pelvic girdle, and ribs, can be detected and separated automatically using approaches presented in Sections III.A and III.B. The results are illustrated in Fig. 14. It is evident that despite small spacing in intervertebral and hip joints, neighboring bones are separated successfully using the splitting filters. The *LAP/HEH* splitting filter demonstrates robust performance in separating bones in the low-resolution μCT volumes depicted in Fig. 14. Majority of the skeletal bones including pelvis, femur, tibia, patella, and lower vertebrae are successfully separated despite large voxel size and low resolution. These results substantiate the robustness of the *LAP/ HEH* splitting filter in separating bones at lower μCT resolutions (40-80 μm voxel size).

For wide-FOV datasets, the morphometry or mineral density of individual bones can be quantified upon separation. For long bones, slice-by-slice stereological measurements can also be performed on each individual bone. Using the approach described in Section III.D, the stereological measurements can be automatically guided using the bone medial axes. This improves the accuracy of cross-sectional measurements for curved bones. In Fig. 15, the medial axis and a set of normal slices are illustrated for a tibia from the μCT volume presented in Fig. 14(a). Using slices normal to the medial axis, automated stereological measurements are applied to cross-sections along the longitude of the bone as discussed in Section III.D.

For proof of concept, stereological measurements were performed using medial axis guidance on the tibia in Fig. 15 which is from a healthy murine model. These slice-by-slice measurements included area moments of inertia and cortical and total cross-sectional area. The results are listed in Table II.

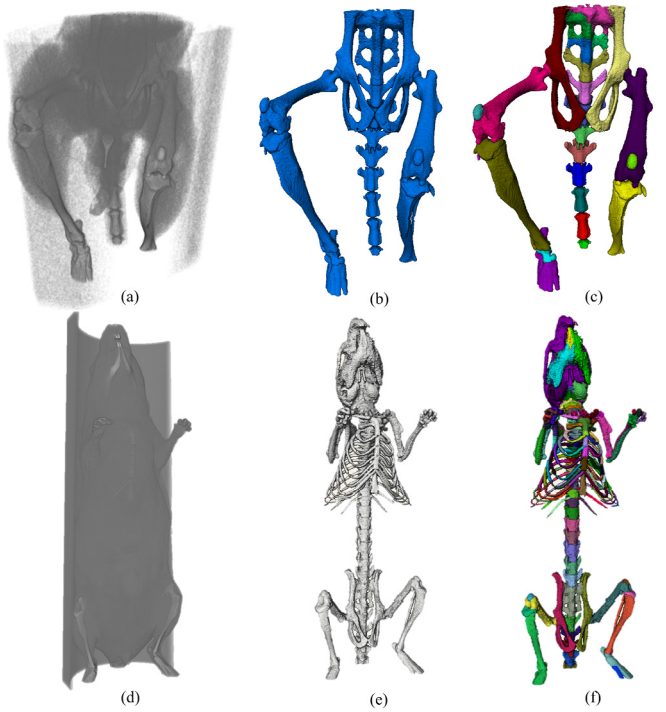

Fig. 14. Bone detection and separation are applied to wide-FOV μCT scans of the hind limbs and whole body of healthy murine models. The hind limbs are scanned at an FOV of 30 mm and voxel size of 58 μm. The whole body scan is at an FOV of 90 mm and voxel size of 72 μm. The grayscale volumes are illustrated in parts (a) and (d). The detected bone masks are illustrated in parts (b) and (e) which similar to the results in Fig. 4, show a robustly detected ischium. The bone separation results are depicted in parts (c) and (f). It can be seen that the long bones, including femur and tibia, and lower and upper vertebrae are correctly separated. There are some inaccuracies in middle vertebrae which are a result of extremely thin spacing in the joints compounded by low spatial resolution.

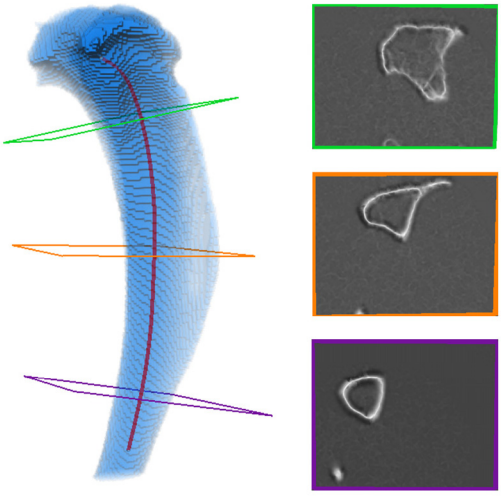

Fig. 15. The medial axis, characterized for a tibia from the μCT volume in Fig. 14(a), guides the slice-by-slice stereological measurements. The cross sections of the bone are extracted based on planes normal to the medial axis as illustrated in three slices from different regions of the bone.

TABLE II
STEREOLOGICAL MEASUREMENTS OF MOUSE TIBIA IN WIDE-FOV DATA

Symbol	Parameter	Measured Value 30 mm FOV 58 μm Voxel Size
Ct.Ar	Cortical Area	1.36 mm^2
Tt.Ar	Total Area	1.95 mm^2
I_{yy}	Area Moment of Inertia y-axis	0.286 mm^4
I_{xx}	Area Moment of Inertia x-axis	0.107 mm^4
J	Polar Area Moment of Inertia	0.393 mm^4

V. DISCUSSION AND CONCLUSIONS

Fully automated analysis and measurement of bones in μCT volumes pose significant challenges including splitting of individual bones, separation of metaphysis and epiphysis, and segmentation of bone compartments. In this paper, we demonstrated a comprehensive framework built upon 3D image processing techniques towards automation of bone analysis and measurements. Several novel techniques were used in this framework to overcome the challenges. By automating the analysis workflow, problems associated with human operator dependency including inconsistency, bias, irreproducibility, and inaccuracy are avoided.

It was shown that rotationally invariant hybrid *LAP/HEH* splitting filters can provide accurate automated bone separation. For small-FOV scans (10 mm and smaller) with high spatial resolution (voxel size of 20 μm or smaller), the automated bone separation splits all the bones, including small joint nodules, without error. This could be seen by visual comparison of the results presented in Figs. 12(e), 12(f), 12(g), 12(h) with the musculoskeletal atlas of murine models [30]. Additionally, the epiphysis and metaphysis sections of long bones can also be automatically separated using hybrid *LAP/HEH* splitting filters. This was shown for long bones, *i.e.*, femur and tibia, in *in vivo* scans of murine knee joints as depicted in Figs. 12(g) and 12(h). Manual separation of metaphysis and epiphysis of long bones is an extremely laborious task and prone to human error [23], [24]. It has been shown that *LAP/HEH* automated bone splitting provides improved accuracy in addition to speed and automation in comparison with manual separation [24]. As such, automating the separation significantly improves the speed and reliability of the analysis. Using *LEH* filters, it was shown that the growth plate of long bones can be excluded from analysis as depicted in Figs. 8 and 13. This further enhances the fidelity of morphometric measurements of cortical and cancellous compartments of long bones.

For wide-FOV scans (larger than 10 mm), bone detection and separation become challenging because the resolution is low and partial volume effects are more pronounced. It was shown that using a hybrid thresholding scheme, the bone tissue can be accurately segmented from soft tissue. This is substantiated by comparing the hybrid thresholding result in Fig. 4 to the traditional global thresholding result in Fig. 1(b). Additionally, by comparing the bone detection results in Figs. 12 and 14 to the murine musculoskeletal atlas [30], the accuracy of the hybrid thresholding can be confirmed. For bone separation, the hybrid *LAP/HEH* splitting filters provide reliable performance. Most notably, the thin spacing in hip and vertebral joints creates challenges for automated separation. As illustrated in Figs. 14(c) and 14(f), bone separation successfully separates long bones, including tibia and femur, pelvic girdle, and lower and upper vertebrae in wide-FOV scans. However, the very thin joints of middle vertebrae make their splitting challenging in low-resolution scans (voxel size of 40 μm and larger). The suboptimal splitting in the middle vertebrae in Fig. 14(c) and the under-separation of middle vertebrate in Fig. 14(f) are due to the challenge of splitting extremely thin joints at low μCT resolutions.

The bone separation algorithm can be optimized by adjusting the cut-off levels in the splitting filters. The optimal cut-off levels increase as the spatial resolution drops. In scans with low resolution, *i.e.*, voxel sizes of 40 μm or larger where bone separation is considerably difficult, adjusting the power of splitting can overcome the separation challenge. The side effect of applying splitting filters with high cut-off values is that additional unwanted separation may occur within individual bones. Over-separation of bones occurs frequently in low-resolution μCT volumes at threshold values of the cut-off parameters of the splitting filters granting full separation of all the individual bones. This extra splitting, however, can be easily rectified by user guidance. Compared to existing user-guided workflows that require time-consuming manual operations such as wall drawing [23], instructing the algorithm to join multiple separated components is significantly easier, straightforward, and minimally prone to operator inconsistency and error.

A significant fraction of studies using wide-FOV μCT scans are focused on bone mineral density quantification of single bones. To this end, the automated detection and separation of individual bones is very useful. Studies involving quantification of bone morphometry, including volume, area, and thickness, also significantly benefit from the automated framework as demonstrated in Section IV. For stereological measurements performed along the longitude of long bones, such as area moments of inertia, use of medial axis characterization leads to improved fidelity and reliability in the analysis.

To demonstrate speed advantages of the techniques discussed in this work for performing automated streamlined bone analysis, the computation times required for the image processing algorithms discussed in Section III were analyzed. Computation times were recorded for each step of the workflow in obtaining the results presented in Section IV. As discussed in Section IV, μCT volumes with a range of FOVs (5 mm, 10 mm, 30 mm) and voxel sizes (10 μm, 20 μm, and 58 μm) were used for validation in this work. This speed analysis was performed on a laptop computer with a quad-core i7 2.90 GHz processor running Windows 10 (64-bit). The results are listed in Table III.

Bone detection is performed using hybrid thresholding as discussed in Section III. As a result, its computation time depends directly on what fraction of the μCT volume is taken

TABLE III
COMPUTATION TIMES OF THE AUTOMATED BONE ANALYSIS WORKFLOW STEPS

Process	5 mm FOV 10 µm Voxel Size	10 mm FOV 20 µm Voxel Size	30 mm FOV 58 µm Voxel Size
Bone Detection	41.1 s	33.2 s	28.7 s
Bone Separation	65.7 s	58.3 s	57.54 s
Compartment Segmentation	38.4 s	35.2 s	N/A
Growth Plate Exclusion	8.1 s	5.9 s	N/A
Medial Axis Characterization	N/A	N/A	21.5 s

up by bone voxels. Higher bone fraction results in slower computation time as the local thresholding operation must be performed in a higher number of voxels. As listed in Table III, the computation times for bone detection drop as the FOV increases. It must be noted that if the local thresholding operation in hybrid thresholding is not limited to the preliminary bone mask, the computation times increase from around 40 s (for a μCT volume at 5 mm FOV) to approximately 480 s. This is because the threshold extrapolation, which is one of the most computationally expensive operations in bone detection, must recursively calculate thresholds for the entire μCT volume. For bone separation, the computation time is dominated by the marker-controlled watershed operation and calculation of the *LAP*/*HEH* splitting filter. Bone separation has the longest computation time among the workflow steps, as listed in Table III, which is expected considering the complexity of its numerical operations. The compartment segmentation primarily involves morphological image processing operations and it is slightly faster than bone detection and separation steps. The growth plate exclusion has one main operation which is *LEH* filtering. As such, its computation time is faster than the other steps. The medial axis characterization is only applicable to curved long bones in FOVs larger than 10 mm. Its computation time is mainly attributes to the 3D skeletonization. The pruning and smoothing operations have lower computational complexity compared to skeletonization.

In conclusion, a fully automated hands-off 3D image analysis framework was presented for volumetric and stereological morphometric measurements of individual bones and bone compartments in μCT volumes. It was shown that using the methodology presented in this paper, the challenges associated with automating bone analysis, especially for *in vivo* μCT scans, can be overcome.

REFERENCES

[1] C. M. Bagi *et al.*, "The use of micro-CT to evaluate cortical bone geometry and strength in nude rats: Correlation with mechanical testing, pQCT and DXA," *Bone*, vol. 38, no. 1, pp. 136–144, 2006.

[2] S. Botter *et al.*, "Quantification of subchondral bone changes in a murine osteoarthritis model using micro-CT," *Biorheology*, vol. 43, pp. 379–388, Jan. 2006.

[3] P. Guggenbuhl, F. Bodic, L. Hamel, M. Baslé, and D. Chappard, "Texture analysis of X-ray radiographs of iliac bone is correlated with bone micro-CT," *Osteoporosis Int.*, vol. 17, no. 3, pp. 447–454, 2006.

[4] D. W. Holdsworth and M. M. Thornton, "Micro-CT in small animal and specimen imaging," *Trends Biotechnol.*, vol. 20, no. 8, pp. S34–S39, 2002.

[5] Y. Jiang, J. Zhao, E.-Y. Liao, R.-C. Dai, X.-P. Wu, and H. K. Genant, "Application of micro-CT assessment of 3D bone microstructure in preclinical and clinical studies," *J. Bone Mineral Metabolism*, vol. 23, pp. 122–131, Jan. 2005.

[6] A. C. Jones, C. H. Arns, A. P. Sheppard, D. W. Hutmacher, B. K. Milthorpe, and M. A. Knackstedt, "Assessment of bone ingrowth into porous biomaterials using MICRO-CT," *Biomaterials*, vol. 28, no. 15, pp. 2491–2504, 2007.

[7] R. D. Kapadia *et al.*, "Applications of micro-CT and MR microscopy to study preclinical models of osteoporosis and osteoarthritis," *Technol. Health Care*, vol. 6, pp. 361–372, Jan. 1998.

[8] B. Van Rietbergen *et al.*, "Assessment of cancellous bone mechanical properties from micro-FE models based on micro-CT, pQCT and MR images," *Technol. Health Care*, vol. 6, pp. 413–420, Jan. 1998.

[9] L. A. Feldkamp, S. A. Goldstein, M. A. Parfitt, G. Jesion, and M. Kleerekoper, "The direct examination of three-dimensional bone architecture *in vitro* by computed tomography," *J. Bone Mineral Res.*, vol. 4, no. 1, pp. 3–11, 1989.

[10] V. David *et al.*, "Noninvasive *in vivo* monitoring of bone architecture alterations in hindlimb-unloaded female rats using novel three-dimensional microcomputed tomography," *J. Bone Mineral Res.*, vol. 18, no. 9, pp. 1622–1631, 2003.

[11] M. J. Paulus, S. S. Gleason, S. J. Kennel, P. R. Hunsicker, and D. K. Johnson, "High resolution X-ray computed tomography: An emerging tool for small animal cancer research," *Neoplasia*, vol. 2, pp. 62–70, Jan. 2000.

[12] E. L. Ritman, "Molecular imaging in small animals—Roles for micro-CT," *J. Cellular Biochem.*, vol. 87, pp. 116–124, Jan. 2002.

[13] J. Yang, S. M. Pham, and D. L. Crabbe, "High-resolution micro-CT evaluation of mid-to long-term effects of estrogen deficiency on rat trabecular bone 1," *Academic Radiol.*, vol. 10, no. 10, pp. 1153–1158, 2003.

[14] M. L. Bouxsein, S. K. Boyd, B. A. Christiansen, R. E. Guldberg, K. J. Jepsen, and R. Müller, "Guidelines for assessment of bone microstructure in rodents using micro–computed tomography," *J. Bone Mineral Res.*, vol. 25, no. 7, pp. 1468–1486, 2010.

[15] G. Campbell, H. Buie, and S. Boyd, "Signs of irreversible architectural changes occur early in the development of experimental osteoporosis as assessed by *in vivo* micro-CT," *Osteoporosis Int.*, vol. 19, no. 10, pp. 1409–1419, 2008.

[16] J. A. Gasser, P. Ingold, K. Grosios, A. Laib, S. Hämmerle, and B. Koller, "Noninvasive monitoring of changes in structural cancellous bone parameters with a novel prototype micro-CT," *J. Bone Mineral Metabolism*, vol. 23, no. 1, pp. 90–96, 2005.

[17] A. Laib, O. Barou, L. Vico, M. H. Lafage-Proust, C. Alexandre, and P. Rügsegger, "3D micro-computed tomography of trabecular and cortical bone architecture with application to a rat model of immobilisation osteoporosis," *Med. Biol. Eng. Comput.*, vol. 38, no. 3, pp. 326–332, 2000.

[18] A. J. Ramme *et al.*, "Automated bone segmentation and surface evaluation of a small animal model of post-traumatic osteoarthritis," *Ann. Biomed. Eng.*, vol. 45, no. 5, pp. 1227–1235, 2017.

[19] R. Müller *et al.*, "Morphometric analysis of human bone biopsies: A quantitative structural comparison of histological sections and micro-computed tomography," *Bone*, vol. 23, no. 1, pp. 59–66, 1998.

[20] M. P. Schwartz and R. R. Recker, "Comparison of surface density and volume of human iliac trabecular bone measured directly and by applied stereology," *Calcified Tissue Int.*, vol. 33, no. 1, pp. 561–565, 1981.

[21] A. M. Parfitt *et al.*, "Bone histomorphometry: Standardization of nomenclature, symbols, and units: Report of the ASBMR Histomorphometry Nomenclature Committee," *J. Bone Mineral Res.*, vol. 2, no. 6, pp. 595–610, 1987.

[22] J. S. Thomsen, A. Laib, B. Koller, S. Prohaska, L. Mosekilde, and W. Gowin, "Stereological measures of trabecular bone structure: Comparison of 3D micro computed tomography with 2D histological sections in human proximal tibial bone biopsies," *J. Microscopy*, vol. 218, no. 2, pp. 171–179, 2005.

[23] AnalyzeDirect, Inc. *Bone Microarchitecture Analysis Add-On*, accessed on Jun. 2017. [Online]. Available: http://analyzedirect.com/analyze-add-ons/bone-analysis-add-on/

[24] J.-C. Tseng, A. Behrooz, J. Meganck, J. Kempner, and J. D. Peterson, "MicroCT investigation of bone erosion and deformation in an osteoarthritic rat model," PerkinElmer, Inc., Hopkinton, MA, USA, Appl. Note 012746A_01, May 2016.

[25] T. Kohler, M. Beyeler, D. Webster, and R. Müller, "Compartmental bone morphometry in the mouse femur: Reproducibility and resolution dependence of microtomographic measurements," *Calcified Tissue Int.*, vol. 77, no. 5, pp. 281–290, 2005.

[26] T. Hildebrand and P. Rüegsegger, "A new method for the model-independent assessment of thickness in three-dimensional images," *J. Microscopy*, vol. 185, no. 1, pp. 67–75, 1997.

[27] N. Otsu, "A threshold selection method from gray-level histograms," *Automatica*, vol. 11, nos. 285–296, pp. 23–27, 1975.

[28] J. H. Waarsing, J. S. Day, and H. Weinans, "An improved segmentation method for *in vivo* μCT imaging," *J. Bone Mineral Res.*, vol. 19, no. 10, pp. 1640–1650, 2004.

[29] S. Beucher and F. Meyer, "The morphological approach to segmentation: The watershed transformation," *Opt. Eng.*, vol. 34, pp. 433–481, Jan. 1993.

[30] I. A. Bab, C. Hajbi-Yonissi, Y. Gabet, and R. Müller, *Micro-Tomographic Atlas of the Mouse Skeleton*. New York, NY, USA: Springer, 2007.

[31] H. R. Buie, G. M. Campbell, R. J. Klinck, J. A. MacNeil, and S. K. Boyd, "Automatic segmentation of cortical and trabecular compartments based on a dual threshold technique for *in vivo* micro-CT bone analysis," *Bone*, vol. 41, no. 4, pp. 505–515, 2007.

[32] W. A. Kalender, *Computed Tomography: Fundamentals, System Technology, Image Quality, Applications*. Hoboken, NJ, USA: Wiley, 2011.

[33] M. Nixon, *Feature Extraction and Image Processing*. San Francisco, CA, USA: Academic, 2008.

[34] M. B. Dillencourt, H. Samet, and M. Tamminen, "A general approach to connected-component labeling for arbitrary image representations," *J. ACM*, vol. 39, no. 2, pp. 253–280, Apr. 1992.

[35] K. Parvati, B. S. P. Rao, and M. M. Das, "Image segmentation using gray-scale morphology and marker-controlled watershed transformation," *Discrete Dyn. Nature Soc.*, vol. 2008, 2008, Art. no. 384346, doi: 10.1155/2008/384346.

[36] M. Doube *et al.*, "BoneJ: Free and extensible bone image analysis in ImageJ," *Bone*, vol. 47, no. 6, pp. 1076–1079, 2010.

[37] T. C. Lee, R. L. Kashyap, and C. N. Chu, "Building skeleton models via 3D medial surface axis thinning algorithms," *CVGIP, Graph. Models Image Process.*, vol. 56, no. 6, pp. 462–478, 1994.

[38] M. Sato, I. Bitter, M. A. Bender, A. E. Kaufman, and M. Nakajima, "TEASAR: Tree-structure extraction algorithm for accurate and robust skeletons," in *Proc. 8th Pacific Conf. Comput. Graph. Appl.*, 2000, pp. 281–449.

[39] N. Miyahara, T. Kokubo, Y. Hara, A. Yamada, T. Koike, and Y. Arai, "Evaluation of X-ray doses and their corresponding biological effects on experimental animals in cone-beam micro-CT scans (R-mCT2)," *Radiol. Phys. Technol.*, vol. 9, no. 1, pp. 60–68, 2016.

[40] D. Giordano, R. Leonardi, F. Maiorana, G. Scarciofalo, and C. Spampinato, "Epiphysis and metaphysis extraction and classification by adaptive thresholding and DoG filtering for automated skeletal bone age analysis," in *Proc. 29th Annu. Int. Conf. IEEE Eng. Med. Biol. Soc.*, Aug. 2007, pp. 6551–6556.